A PHYSICS-BASED APPROACH TO URBAN AIR MOBILITY

Patricia Ventura Diaz, patricia.venturadiaz@nasa.gov, NASA Ames Research Center (United States)
Seokkwan Yoon, s.yoon@nasa.gov, NASA Ames Research Center (United States)

Abstract

High-fidelity Computational Fluid Dynamics (CFD) simulations for multi-rotor vehicles have been carried out. The three-dimensional unsteady Navier-Stokes equations are solved on overset grids employing high-order accurate schemes, dual-time stepping, and a hybrid turbulence model using NASA's CFD code Over-flow. The vehicles studied consist of small to medium sized drones, and bigger vehicles for future Urban Air Mobility (UAM) applications. The performances for different configurations and rotor mounting are calculated in hover and in forward flight. Understanding the complex flows and the interactions between rotors and with other elements will help design the future multi-rotor vehicles to be quieter, safer, and more efficient.

NOMENCLATURE

a	Fluid speed of sound
A	Rotor disk area, πR^2
c_{tip}	Rotor blade tip chord length
C_Q	Torque coefficient, $\frac{Q}{\rho(\Omega R)^2 RA}$
C_T	Thrust coefficient, $\frac{T}{\rho(\Omega R)^2 A}$
d	Turbulent length scale
FM	Figure of merit, $\frac{C_T^{3/2}}{\sqrt{2}C_Q}$
M_{tip}	Blade tip Mach number, $\frac{\Omega R}{a}$
NB	Near-body
OB	Off-body
Q	Rotor torque
r	Radial position
R	Rotor radius
Re	Reynolds number, $\frac{V_{tip}c_{tip}}{\nu}$
T	Rotor thrust
V	Velocity magnitude
V_∞	Flow velocity
y^+	Non-dimensional viscous wall spacing
α	Angle of attack, AoA
δ	Boundary layer thickness
Δ	Grid spacing
μ	Advance ratio, $\frac{V_\infty cos(\alpha)}{\Omega R}$
ν	Fluid kinematic viscosity
ρ	Fluid density
Ω	Rotor rotational speed

1. INTRODUCTION

Small and medium-sized multi-rotor craft like Unmanned Aerial Vehicles (UAVs) have grown very popular over the last decade. While originally UAVs were designed for military applications, their use has rapidly expanded to the civil market. The unique ability of vertical lift vehicles to hover has great potential for human and cargo transportation, delivery systems, surveillance missions, disaster relief, and even planetary exploration. Compared to single rotor systems, multi-rotor vehicles offer an advantage in lifting capacity because the size of a single rotor is limited by the tip speed and structural mechanics. Instead, multiple rotors can be employed with reduced tip Mach number and aeroelastic effects.

Accurate prediction of rotorcraft performance and acoustics continues to be challenging. The flows are inherently unsteady, nonlinear, and complex. For instance, a rotor blade can encounter its own tip vortex and the tip vortices of other blades. It is even more difficult when there are aerodynamic interactions between multiple rotors and fuselage because of the close proximity of all of these components. High-fidelity Computational Fluid Dynamics (CFD) methods offer an advantage over low-fidelity tools when investigations of the interactional aerodynamics of multi-rotor craft are required.

Since unmanned vehicles are sized and optimized for particular missions, modern low-fidelity conceptual design and sizing tools that have been used for the design of large helicopters can also be used for the design of multi-rotor craft. However, there are aerodynamic features of these multi-rotor vehicles that can be difficult to account for with these low-fidelity tools, unless there is a method to calibrate the tools. High-fidelity CFD can provide the information needed to calibrate low-fidelity design tools to account for aerodynamic interactions.

More recently, the concept of Urban Air Mobility (UAM) has been mentioned by both large and small companies asserting that commute times would be drastically reduced by using UAM vehicles (popularly known as "flying cars"). UAM vehicles are en-

visioned to be autonomous and use electric or hybrid propulsion, to transport a small number of passengers from one point in a city to another in a short time, avoiding all ground traffic, and to have the capacity of Vertical Take-Off and Landing (VTOL), eliminating the need for large-scale infrastructure such as long runways. Their rechargeable batteries promise a greener future for aviation. New autonomy research and air traffic management efforts at NASA have the potential to provide the "flying roads" and manage the traffic of UAM vehicles in urban areas.

Still, UAM has to ensure safe, quiet, and efficient vehicles in order to be able to fly in our cities. The objective of the present work is to demonstrate a high-fidelity simulation capability to study the complex interactional aerodynamics of multi-rotor vehicles for different flight conditions and configurations and to establish the good practice in the design of multi-rotor UAVs and multi-rotor craft for UAM.

Three drones, described below, have been studied: the DJI Phantom 3, the SUI Endurance, and the Elytron 4S UAV; see Ventura et al.[1,2] and Yoon et al.[3,4]. NASA's UAM conceptual design for VTOL air taxi operations is also shown in this study, see Johnson et al.[5]. The vehicles are simulated using NASA's high-order accurate CFD solver, Overflow, and their complex flowfields and performance in different configurations are analyzed and compared. The geometries have been modeled with a extraordinary level of detail and accuracy when comparing to the real vehicles, yielding to state-of-the-art high-fidelity CFD results.

1.1. The DJI Phantom 3

Figure 1: DJI Phantom 3 quadcopter.

The DJI Phantom 3 is an example of a classic commercial quadcopter design with a symmetric X-shaped airframe, see figure 1. It can be used to hover above static or slow-moving objects, to record high quality videos for example. Overset grids have been generated for the complete DJI Phantom 3, which consists of the X-shaped airframe, four rotors, the landing gear, the camera and the battery. The effect of over- and undermounting the rotors in hover is calculated with CFD simulations. Results for an octocopter concept are shown. Then, a simplified airframe is compared with the complete airframe in order to asses the effect of components (landing gear, battery, camera). Finally, the effects of wind gusts on the quadcopter during hover are presented.

1.2. The SUI Endurance

Figure 2: SUI Endurance quadcopter.

The SUI Endurance is an example of a forward-flight quadcopter design with an elongated airplane-like airframe that can be used for missions in which the UAV will be operating during most of its flight envelope in forward-flight mode, see figure 2. Thus, it is designed for faster speeds in forward flight than a regular quadcopter, and it can be used for cargo transportation or video recording of fast-moving objects. This study focuses on the performances and characteristics of the flow in forward flight for the SUI Endurance. Three configurations are studied here, in order to see the effect of over- and undermounted rotors on aerodynamic efficiency. The first configuration, the SUI standard, is the original configuration for the SUI Endurance UAV, where the four rotors are overmounted. In the second configuration, the SUI hybrid, the fore rotors are undermounted and the aft rotors are overmounted. The third configuration is the SUI undermounted, where all rotors are placed underneath the arms. The performances of the three configurations are compared in forward flight.

1.3. The Elytron 4S UAV

The Elytron 4S UAV — or Elytron for short — is the wind-tunnel-scaled model of the Elytron 4S, a concept vehicle for future UAM, see figure 3 for the

UAM concept, and figure 4 for the UAV wind-tunnel-scaled model.

Figure 3: Elytron joined-wing tilt-wing UAM concept.

Figure 4: Elytron 4S UAV in the US Army 7x10 subsonic wind tunnel at NASA Ames Research Center.

The Elytron design combines three sets of wings: a single tilt-wing in central position with the prop-rotors mounted on it and two pairs of fixed wings. The fixed wings are split into a forward pair and an aft pair that are joined by winglets, thus making use of the joined wing concept, and by a vertical empennage to the fuselage. By splitting the wings apart, the design tries to reduce any interference with the thrust of the prop-rotors. The counter-rotating prop-rotors allow for torque cancellation. The tilt-wings can tilt 90 degrees in order to perform VTOL or "helicopter mode". During forward flight or "airplane mode" the tilt angle is 0 degrees. The nose fan is placed in the front of the vehicle for pitch control and better load distribution during VTOL.

1.4. NASA's Side-by-Side UAM Concept

Urban air taxi operations, also known as UAM applications, are enabled by VTOL capability. Power and energy requirements are minimized by using low disk-loading rotors, and short range requirements permit consideration of non-traditional propulsion concepts.

NASA's side-by-side conceptual design is a six-passenger, 200 nm range helicopter with hybrid propulsion; see figure 5. The intermeshing side-by-side helicopter increases lifting capability while

Figure 5: NASA's side-by-side UAM helicopter concept.

maintaining similar maximum outer vehicle dimensions when compared to a non-intermeshing case. This concept vehicle is intended to focus and guide NASA research activities in support of aircraft development for emerging aviation markets.

2. NUMERICAL APPROACH

The flow solver used in this study is NASA's Overflow[6] CFD solver. Overflow is a finite-difference, structured overset grid, high-order accurate Navier-Stokes flow solver. NASA's Chimera Grid Tools (CGT)[7] overset grid generation software is used for generating the overset grids of rotors and complete vehicles. Body-fitted curvilinear near-body (NB) grids are generated using CGT. The computational domain is completed with the generation of Cartesian off-body (OB) grids that are automatically generated prior to grid assembly using the Domain Connectivity Framework in Overflow-D mode. The current time-accurate approach consists of an inertial coordinate system where NB curvilinear O-grids for the rotor blades rotate through the fixed OB Cartesian grid system.

2.1. Overset Grid Generation

The overset grid generation process using CGT can be divided into the following steps: geometry processing, surface grid generation, volume grid generation, and domain connectivity[7]. The geometry is usually obtained from a CAD model. Overlapping hyperbolic or algebraic surface grids are then generated. The generation of surface grids is the step that requires the most manual effort and experience from the user.

With sufficient overlap between surface grids, the volume grids can be created easily with hyperbolic marching methods out to a fixed distance

from the surface. Such methods provide orthogonal grids with tight clustering characteristics at the wall, which is essential for accurately capturing the boundary layer in viscous flow computations. The distance is chosen such that the outer boundaries of the near-body volume grids are well clear of the boundary layer. The near-body grids are then embedded inside off-body Cartesian grids that extend to the far field.

Surface grid resolution on the rotor blades is clustered in the chordwise direction near the airfoils leading and trailing edges to accurately resolve large pressure gradients. The spanwise resolution is clustered near the root and the tip. There is not an established practice for generating the grids for the airframes, as each case has its own topology. In general, clustering near corners and high curvature regions is good practice. The normal grid spacing at the wall of all grids maintains $y^+ < 1$.
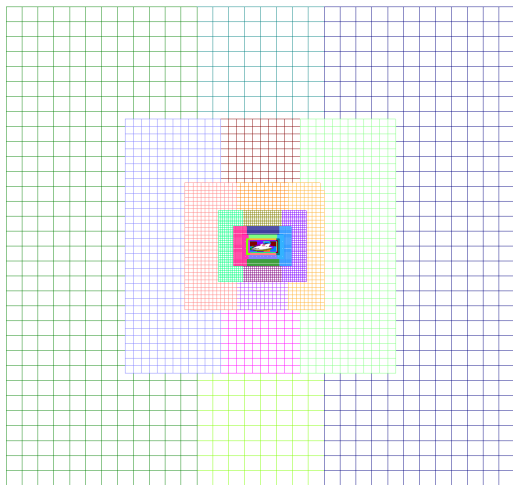
Figure 6: Off-body grids for Elytron 4S UAV.

Off-body Cartesian grids with uniform spacing surround the near-body grids to resolve the wake region of interest. Coarser Cartesian grids efficiently expand the grid system to the far field, where each successive Cartesian grid is twice as coarse as its previous neighbor. The far-field boundary is 20 rotor radii away from the center of the vehicle in all directions. The resolved wake region has a uniform grid spacing of 10% of the tip chord length c_{tip}. Figure 6 shows the OB grid system for the Elytron 4S UAV.

By using a trimmed approach, the domain connectivity step is robust and highly automated: hole cutting is required between components and with the off-body Cartesian grids. In this study, the X-ray hole cutting method is used. An X-ray object is created for every component in the geometry (i.e. the blades, the hubs, the fuselage, the landing gear,

etc.). The user has to supply the list of meshes that each X-ray object is allowed to cut, and an offset distance with which to grow each hole away from the body. The hole cutting process is performed at each time step within the flow solver, allowing for the rotation of the blades relative to the fixed airframe.

2.2. High-Order Accurate Navier-Stokes Solver

The Navier-Stokes equations can be solved using finite differences with a variety of numerical algorithms and turbulence models. In this study, the diagonal central difference algorithm is used with the 4th-order accurate spatial differencing option with matrix dissipation or 5th-order accurate spatial differencing option with scalar dissipation. The physical time step corresponds to 0.25 degree rotor rotation, together with up to 50 dual-time sub-iterations for a 2.5 to 3.0 orders of magnitude drop in sub-iteration residual. This numerical approach and time step were previously validated for various rotor flows[8,9]. In order to reduce the computation time required for a converged solution, the first 1440 steps employ a time step equivalent to 2.5° per time step, yielding 10 rotor revolutions. The time step is then reduced to the equivalent of 0.25° per time step, for which 1440 steps correspond to one rotor revolution.

2.3. Low Mach Number Preconditioning

One of the challenges for compressible Navier-Stokes methods in computing small-rotor flows is the relatively low Mach number due to small rotor radii. For example, in the case of the DJI Phantom, the Mach number at the blade tips, M_{tip}, is under 0.2 at 5400 RPM. Mach numbers at the inboard locations are even lower.

Compressible Navier-Stokes codes in general suffer from slow convergence for low speed flows because of a disparity between the acoustic and convective speeds. Because most numerical algorithms have a stability restriction on the size of the time step determined by the maximum eigenvalue, the acoustic speed limits the time step. On the other hand, convergence to a steady state is controlled by the convective speed, which determines how fast low-frequency errors are advected out of the computational domain. If the convective speed is much smaller than the speed of sound, the stability restriction forces time steps so small that convergence requires a large number of iterations. Low Mach number preconditioning[10,11] is an attempt to equilibrate the eigenvalues, making them all of the same order of magnitude and thus decreasing the number of iterations to convergence.

Low Mach number preconditioning is only used during the sub-iteration steps at each physical time step, for vehicles with $M_{tip} \leq 0.2$.

2.4. Hybrid Turbulence Modeling

The Overflow code has a choice of algebraic, one-equation, and two-equation turbulence models, including hybrid Reynolds-Averaged Navier-Stokes / Large Eddy Simulation (RANS/LES) models that close the RANS equations. In this study, the one equation Spalart-Allmaras[12] turbulence model is used primarily within the boundary layer.

The turbulence length scale, d, is defined as the distance from a field point to the nearest wall.

A problem occurs deep within the rotor wake, where d may be several rotor radii in length. In this case, d no longer represents an estimate of the largest turbulent eddy in the local flow but is rather a very large geometric parameter. When d is very large the turbulence dissipation becomes very small. On the other hand, the strong tip vortices in the lower wake can generate significant turbulence production. Over time, this imbalance in turbulence production and dissipation in the lower wake can result in excessively large eddy viscosities. These large viscosities can migrate up the vortex wake after several rotor revolutions and, under blade-vortex interaction conditions, infiltrate the blade boundary layers. When this happens, the rotor blade drag and torque increase significantly and artificially, resulting in an under-prediction of rotor efficiency.

An additional degree of realism can be obtained by the use of LES. In LES, the large turbulent scales are resolved using a small grid spacing Δ, and the smaller scales are modeled. A low-pass spatial filter, associated with a cut-off length, is applied to the Navier-Stokes equations. Below the cut-off length the subgrid-scales must be modeled. However, the use of LES through the entire computational domain is impractical for the Reynolds numbers found in common rotor flows, due to the very small length scales of wall-bounded flows.

The Detached Eddy Simulation (DES) model[12] is a more practical alternative. The intent of DES is to be in RANS mode throughout the boundary layer, where the turbulent scales can be very small and need to be modeled, and in LES mode outside the boundary layer where the largest turbulent scales are grid-resolved. In this way, DES is a RANS/LES hybrid approach that mitigates the problem of artificially large eddy viscosity. The turbulence length scale d is replaced by $\bar{d}$, where $\bar{d}$ is the minimum of the distance from the wall, d, and the local grid spacing times a coefficient.

The DES approach assumes that the wall-parallel grid spacing $\Delta_{\parallel}$ exceeds the thickness of the boundary layer δ so that the RANS model remains active near solid surfaces. If the wall-parallel grid spacing is smaller than the boundary layer thickness, $\Delta_{\parallel} < \delta$, then the DES Reynolds stresses can become under-resolved within the boundary layer; this may lead to non-physical results, including grid-induced separation. Using Delayed Detached Eddy Simulation (DDES)[13], the RANS mode is prolonged and is fully active within the boundary layer. The wall-parallel grid spacing used in this study does not violate the hybrid-LES validity condition; thus DES and DDES should give similar results. Nevertheless, all computations have been performed using the DDES model for both NB and OB grids.

3. RESULTS

In this section, the results obtained for the four vehicles shown in the Introduction are presented: the DJI Phantom 3 in hover, the SUI Endurance in forward flight, the Elytron 4S UAV, and the side-by-side UAM concept.

The Overflow Navier-Stokes CFD code and the Chimera Grid Tools software are used throughout this study. All computations have been carried out with NASA's supercomputers Pleiades and Electra located at the NASA Advanced Supercomputing (NAS) facilities at NASA Ames Research Center.

Each vehicle will be presented in a similar way: the overset grids that model the geometry are introduced first, then the CFD results from Overflow for different configurations will be shown. The effects of the changes in arrangements will be compared, extracting conclusions regarding good practice in the design of multi-rotor VTOL vehicles.

3.1. The DJI Phantom 3 in Hover

The quadcopter DJI Phantom 3 is constructed by incorporating the four rotors to the X-shaped airframe in diagonal-opposed clock-wise (CW) and counter-clock-wise (CCW) positions for torque cancellation.

3.1.1. Overset Grids

The geometries for two different airframes and two different rotor blades have been modeled. The overset grids are generated using CGT following the procedure summarized in section 2.1. For a more complete guide on how to generate high-quality overset grids and the good practices, see Chan et al.[7]. The configurations for the DJI are:

- Floureon's carbon fiber (CF) replica rotor blades; see figure 7 top.

- Original DJI Phantom 3 injection-molded flexible rotor blades; see figure 7 bottom.

- Simplified DJI Phantom 3 airframe; see figure 8. It consists of the CF replica rotors and the X-shaped main body.

- Complete DJI Phantom 3 airframe; see figure 9. It includes the original rotors, X-shaped main body, landing gear, camera and battery.
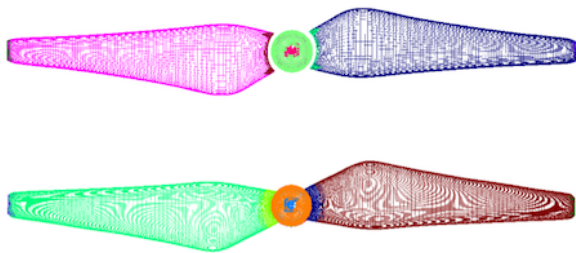

Figure 7: Overset surface grids for Floureon's CF replica blades (top) and the original Phantom 3 blades (bottom).
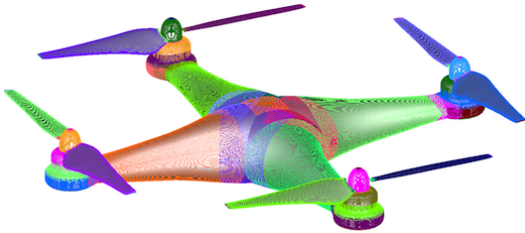
Figure 8: Overset surface grids for the simplified DJI Phantom.

Figure 9: Overset surface grids for the complete DJI Phantom 3.

The simplified airframe has been modeled using high-order polynomials and CAD software. Collar grids are used at the junctions, and cap grids cover singular axis.

Both the CF and original rotor blades and the complete airframe were obtained at NASA Ames using high resolution laser scan techniques. The rotor blades are defined by airfoil profiles at different radii from the point cloud. The profiles are connected and smoothed, obtaining the whole blade. Each rotor system consists of two blades attached to a central hub. O-grids are used for the blades. Cap grids are needed at the blade tips and the axis of the hub. At the junction with the hub, collar grids are used.
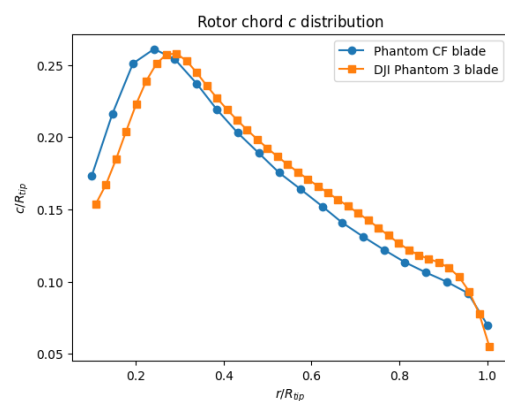
(a) Chord distribution.
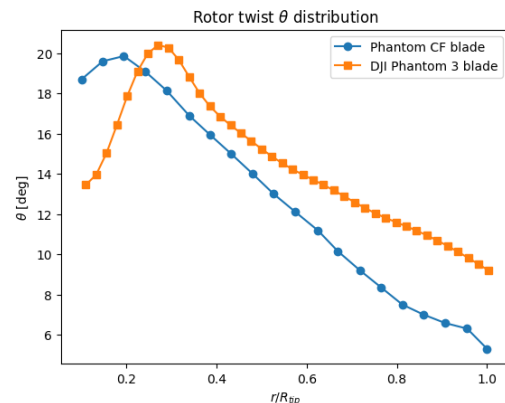
(b) Twist distribution.

Figure 10: Comparison of DJI Phantom 3 factory plastic and CF blades, normalized by the rotor radius R.

Comparisons between the chord and the twist distribution of the two rotor blades are shown in figure 10. Chord length is normalized by the rotor radius. At outboard radial stations where most thrust is generated, the difference in twist is approximately 4 degrees. For comparison of the CF replica

blades with the original blades, the pitch angle for the CF blades is increased by 4 degrees.

The NB volume grids for the complete airframe consist of 202 overset grids, with 29 million grid points. The complete grid system of NB and OB grids has 396 million grid points.

The NB volume grids for the simplified airframe consist of 86 overset grids, with a total of NB and OB 387 million grid points.

3.1.2. DJI Isolated Rotors

The rotational speed in hover for the DJI Phantom 3 was measured in flight test and it is equal to $\Omega_{hover} = 5400$ RPM.
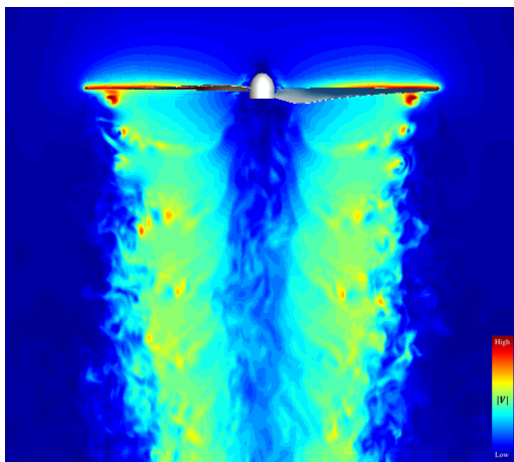
(a) CF replica blades.
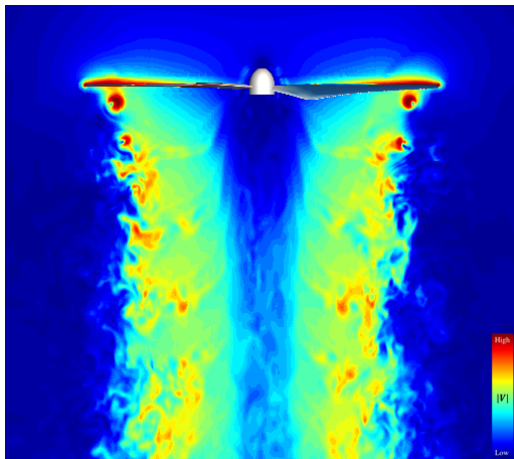
(b) Original blades.

Figure 11: Comparison of the velocity magnitude for the DJI Phantom CF replica blades (a) and the factory plastic blades (b), pressure shown at the surface of the blades.

In previous studies with the CF replica blade[3], a gap was created between the blade and the hub in
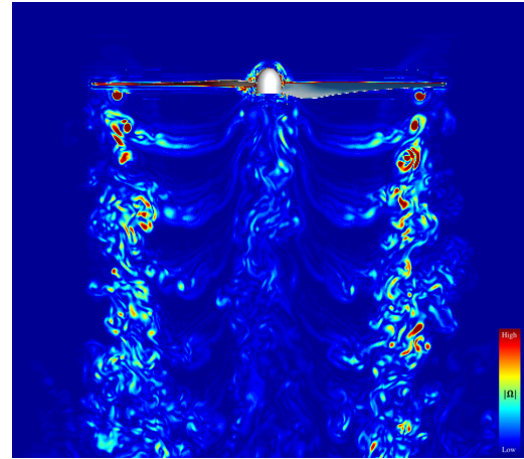
(a) CF replica blades.
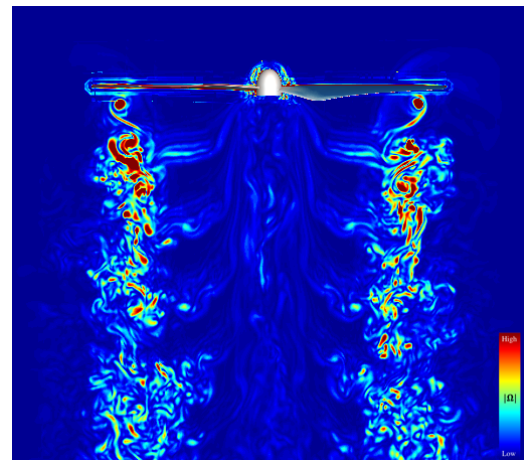
(b) Original blades.

Figure 12: Comparison of the vorticity magnitude for the DJI Phantom CF replica blades (a) and the factory plastic blades (b), pressure shown at the surface of the blades.

order to study the effect of the collective pitch angle on small drone blades, and it was shown that the peak on the figure of merit was obtained for a pitch angle of 8 degrees. However, for comparison of the CF blades with the original blades, the pitch angle is fixed to 4 degrees for all simulations, as mentioned in the previous section. Wind tunnel tests at NASA Ames revealed that the original blades yield higher performance and efficiency than the rigid CF rotor blades[14].

With Overflow, simulations are run for the equivalent of 21 rotor revolutions, reaching convergence of 3.0 orders of magnitude drop in sub-iteration residual, for a quasi-periodic solution. First, the CF replica and original isolated rotors are compared. Figure 11 compares the instantaneous velocity magnitude for the converged solution of the two rotors. The velocity is higher for the original rotors: it is

Presented at 44th European Rotorcraft Forum, Delft, The Netherlands, 18–20 September, 2018.

Page **7** of **21**

an indication that they are more efficient. Figure 12 shows the vorticity magnitude. For Ω_{hover}, the tip Mach number is $M_{tip} = 0.2$, and the Reynolds number is $Re = 37300$.

Table 1 shows the thrust coefficient C_T, the torque coefficient C_Q, and the figure of merit FM for the isolated rotors. The original rotors generate 25% more thrust, and are 6% more efficient for same Ω. The C_T and C_Q are calculated as the mean value of their instantaneous values over the last three revolutions.

	CF replica blades	Original blades
C_T	0.0129	0.0162
C_Q	0.0019	0.0025
FM	0.552	0.585

Table 1: DJI Phantom isolated rotor performances.
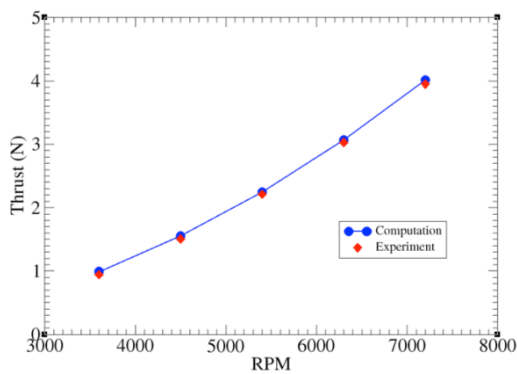
Figure 13: Comparison with experimental data for the DJI Phantom CF rotors for various RPMs

Computational results agree remarkably well with experiments. Figure 13 shows the thrust coefficient for the CF isolated rotor for different Ω. Experimental data was obtained from Zawodny et al.[15].

3.1.3. Effect of Rotor Mounting in Hover

In this section, the simplified airframe is simulated with the CF replica blades* for three rotor-mounting options:

- Overmount, the conventional configuration.

- Undermount, the rotors are placed on the underside of the fuselage arms instead of above. The separation between the rotors and the arms below is the same than with the overmount rotors.

---

*The CF replica rotors were used for this study because when the simulations were run only these rotors were available.

- Off-body undermount. The rotors are at a distance of $0.25R$ below the hub.

A more detailed study can be found in previous work by the authors[3]. Here the most impactful results are summarized.

Figure 14 shows a comparison of velocity magnitude. Of the three configurations, the overmount configuration exhibits the highest speed downwash from the inboard rotor blades, whereas the off-body undermount configuration exhibits the lowest. Figure 15 shows pressure on a vertical plane through the center of the vehicle. While the high pressure below the overmount rotors *pushes down* the fuselage, the low pressure above the undermount rotors *pulls down* the fuselage by almost the same force as the overmount configuration. Compared to the undermount configuration, the fuselage of the off-body undermount configuration experiences much less download. However, without significant interference from the fuselage, the four rotors experience strong interactions among themselves.

Pressure fluctuations on the surface of the vehicle and near it can be observed for the overmount and undermount configurations, being much stronger in the undermount case. For the off-body undermount these fluctuations are weak.

Table 2 shows that the undermount configuration generates 1% less total thrust than the overmount, and the off-body undermount configuration generates 2% less than the undermount configuration. The thrust only from rotors for the off-body undermount is 6% less than the undermount and 7% less than the overmount.

3.1.4. The Octorotor

In order to study the effect of coaxial rotors on the performance of a quadcopter, the configuration has been modified by the addition of four rotors beneath the fuselage. The resulting vehicle configuration employs eight rotors and the simplified airframe. The lower rotors rotate in opposite direction than the upper rotors, that is the rotors are counter-rotating, common practice in coaxial helicopters for torque cancellation. The total number of NB and OB grid points for the vehicle system is 250 million.
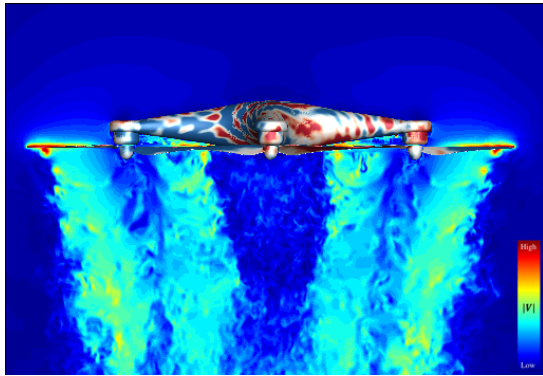
Figures 14 (d) and 15 (d) show the velocity magnitude and the pressure for the torque-balanced octorotor[4]. Note stronger pressure fluctuations on the surface of the vehicle and nearby, than in the quadcopter configurations seen in the previous section.

Rotor positions are in phase. Mounting rotors both above and below arms can increase the thrust
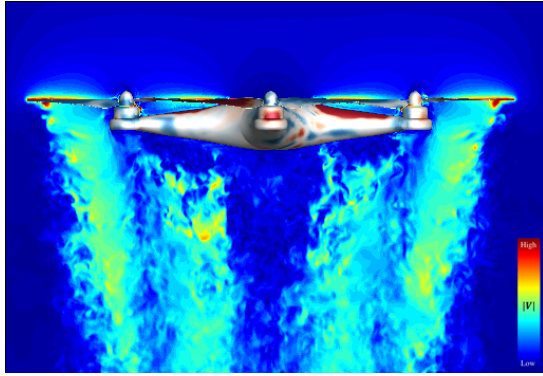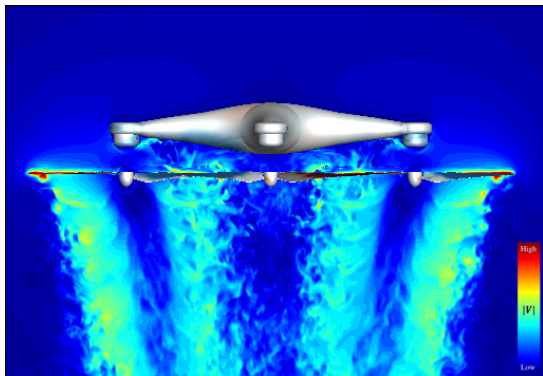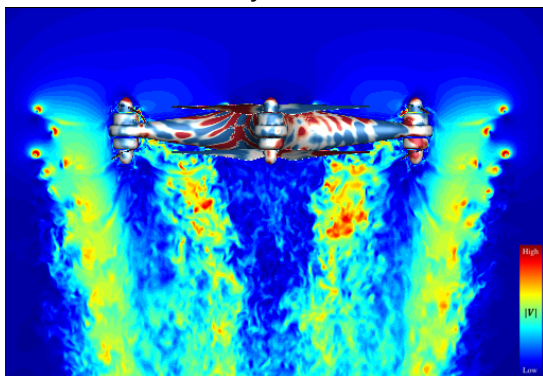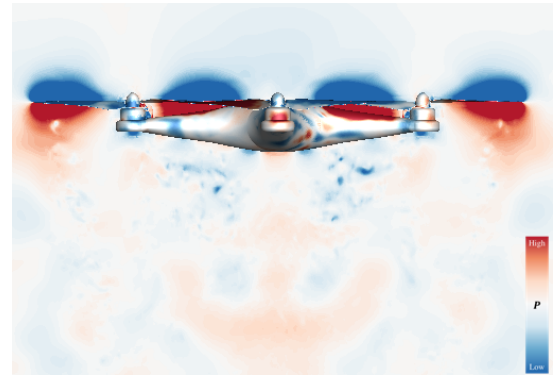
(a) Overmount.

(a) Overmount.

(b) Undermount.

(b) Undermount.

(c) Off-body undermount.

(c) Off-body undermount.
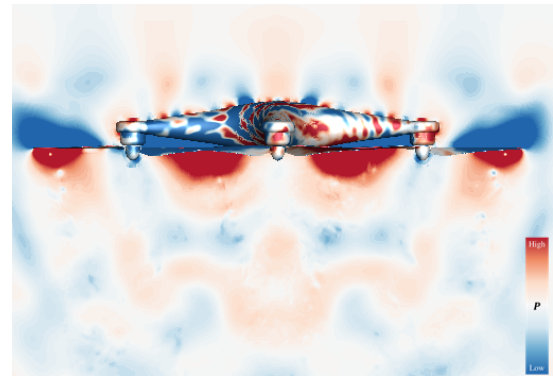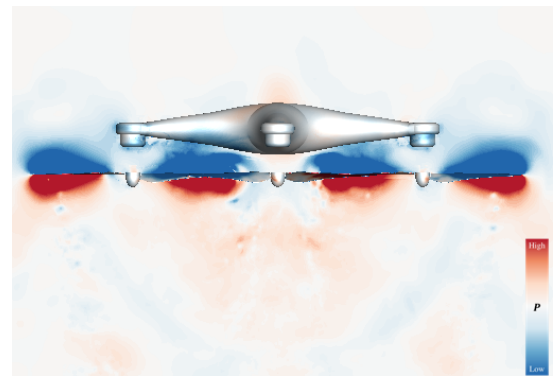

(d) Octorotor.

(d) Octorotor.

Figure 14: Velocity magnitude for overmount (a), undermount (b), off-body undermount (c), and octorotor (d). Pressure shown at the surface.
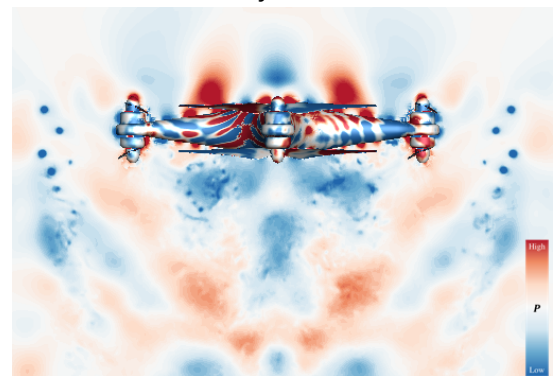
Figure 15: Pressure for overmount (a), undermount (b), off-body undermount (c), and octorotor (d). Pressure shown at the surface.

significantly, but by losing up to 41% efficiency[†]. Yoon et al.[4] showed that the torque-balanced vehicle generates 82% more thrust than the quadcopter, see table 2.

	$C_{T,rot}$	$C_{T,fus}$	$C_{T,tot}$
Overmount	1.025	-0.076	0.949
Undermount	1.016	-0.080	0.936
OB Undermount	0.954	-0.038	0.916
Octorotor Coaxial	1.883	-0.154	1.729
Overmount orig blade	1.263	-0.085	1.178
Complete orig blade	1.268	-0.100	1.168

Table 2: Rotor thrust $C_{T,rot}$, fuselage download $C_{T,fus}$, and total thrust $C_{T,tot}$, for various quadrotor configurations (Forces have been normalized by $4x$ the CF isolated single rotor thrust).

3.1.5. Effects of Adding Components

In order to simulate the real configuration and the effects of additional components, the battery, the landing gear, and a camera, are included in the model of the DJI Phantom 3, see figure 9. Figure 16 shows the velocity contours. The complete configuration exhibits higher velocities in the rotor wake. This is in agreement with the results from isolated rotors: the complete configuration has the original rotors that perform better than the CF replica rotors.
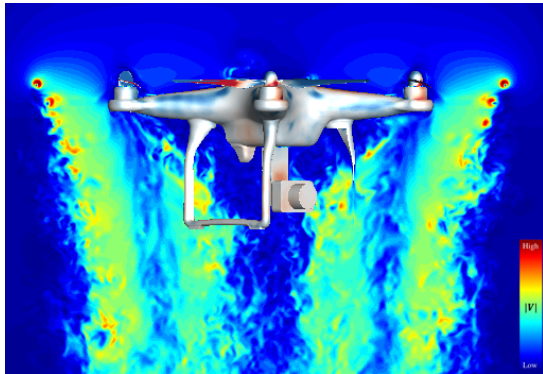
Figure 16: Velocity for complete DJI Phantom 3 with original rotors. Pressure shown at the body surface.

The components block the rotor-rotor interactions underneath the fuselage, increasing the rotor thrust, see table 2. However some of these components are in the rotor wake, and thus they are being *pushed down*, increasing the fuselage download. Overall, the complete vehicle generates 23%

more thrust. When comparing the simplified airframe with the complete airframe both using the same rotors (the original rotors), the complete vehicle generates 1% less thrust. The effect of the components is negative even if the interactions are decreased, because the download is increased more, see Ventura et al.[1] for the full study.

3.1.6. Effect of Wind Gusts

Small quadcopters, and UAVs in general, have poor stability in wind gusts due to the generation of a strong pitching moment when a sudden wind impacts the vehicle.
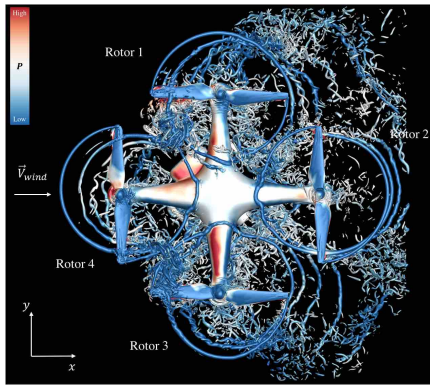
Figure 17 shows the Q-criterion and the pressure on the surfaces for two different wind gust velocities V_{wind} and two incoming angles. When the gust impacts the vehicle, there is a dissymmetry in the flow around the rotors as the rotors see different velocities. This causes an imbalance in the thrust generated, producing a pitching moment. Figures 18 (a) and (b) show the thrust produced by each rotor as a function of the wind velocity, for two incoming angles: through a rotor and from the side. The pitching moment c_x and rolling moment c_y are calculated around the center of gravity. The moment is greater for increasing V_{wind}, as shown in figures 18 (c) and (d).
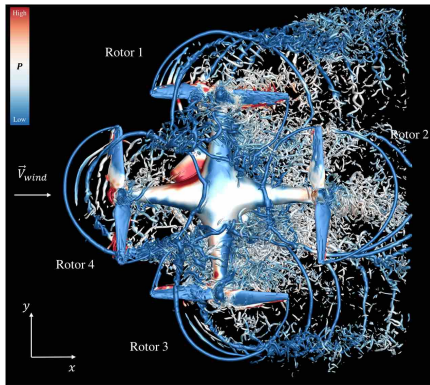
3.2. The SUI Endurance in Forward Flight

The second vehicle presented in this work is the SUI Endurance. The SUI quadcopter's original geometry has been slightly modified for the aerodynamic simulations, by removing, for example, the interior parts or the small pieces used to fold the arms, which do not change the main flow. The aerodynamic SUI configuration consists of the fuselage, four rotors, four arms, four motors, camera mounting, and landing gear. Again, the rotors are added so that there are two diagonally opposed rotors that rotate CW and the other two diagonally opposed rotors rotate CCW. The rest of the vehicle (fuselage, four arms, four motors, and landing gear) has been represented using a CAD model of the SUI quadcopter, provided by SUI to NASA Ames.
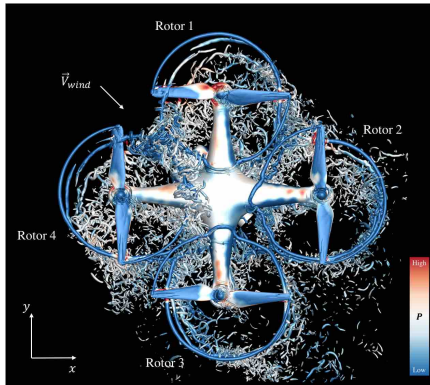
3.2.1. Overset Grids

The quadcopter is constructed by adding to the fuselage two fore arms and two aft arms, each arm supporting at its end the motor and the rotor blades. The fore and aft arms form an angle of 60 and 30 degrees with the fuselage longitudinal axis, respectively. The left fore blades, left aft
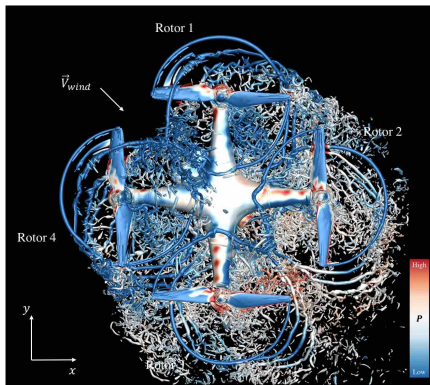

[†]The interference-induced power in coaxial rotors is $\sqrt{2}$, which is a 41% increase in induced power relative to the power required to operate the two rotors in complete isolation.

(a) $V_{wind} = 10 \, kts, \beta = 0°$.

(b) $V_{wind} = 20 \, kts, \beta = 0°$.

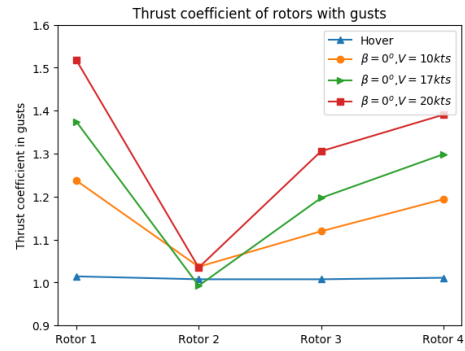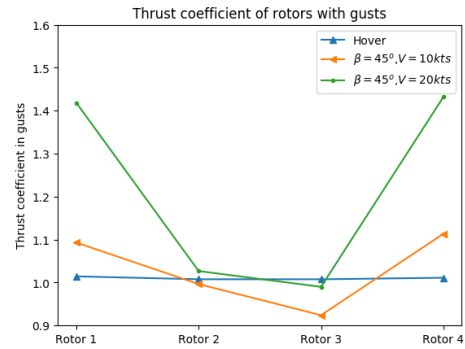(c) $V_{wind} = 10 \, kts, \beta = 45°$.

(d) $V_{wind} = 20 \, kts, \beta = 45°$.
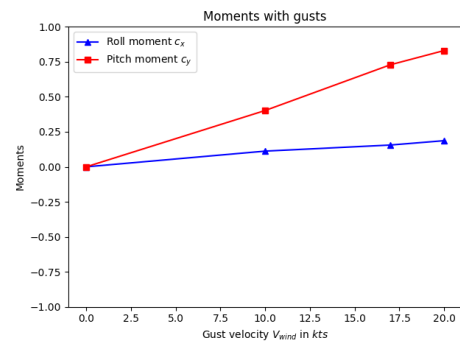
Figure 17: DJI Phantom 3 quadcopter under the effect of wind gusts, for an incoming wind gust through a rotor, $\beta = 0°$, and from the side, $\beta = 45°$.
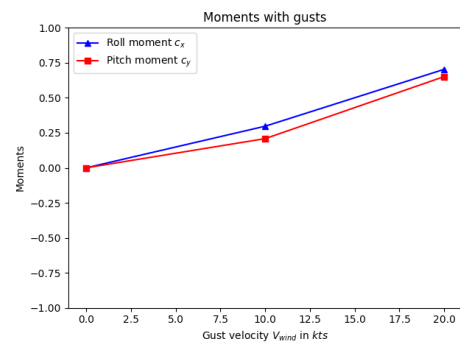

(a) C_T of each rotor, $\beta = 0°$.

(b) C_T of each rotor, $\beta = 45°$.

(c) Moments of each rotor, $\beta = 0°$.

(d) Moments of each rotor, $\beta = 45°$.

Figure 18: Thrust coefficient and moment coefficients of each rotor under the effect of wind gusts, for an incoming wind gust through a rotor, $\beta = 0°$, and from the side, $\beta = 45°$. Forces are normalized by the DJI Phantom 3 original isolated single rotor thrust. Moments are normalized by the thrust times the length of the arm of the airframe.
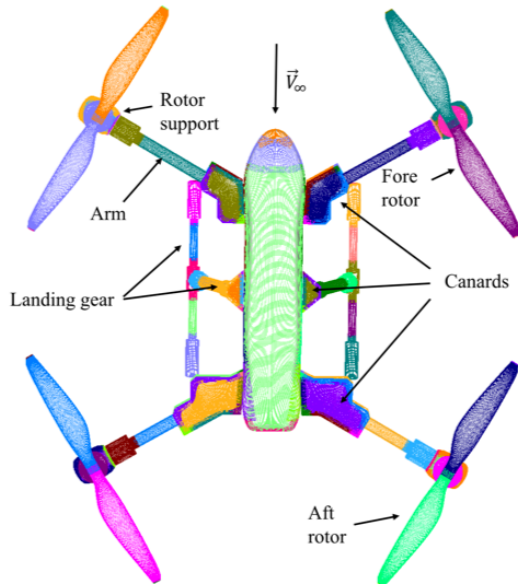
Figure 19: SUI Endurance overset surface grids top view, with the components.

(a) Standard SUI.

(b) Hybrid SUI.

(c) Undermount SUI.

Figure 21: Overset surface grids for different rotor mountings in the SUI Endurance.

blades, right aft blades, and right fore blades (pilot view) rotate CW, CCW, CW and CCW, respectively. The landing gear is also added to the fuselage.

There are 41 million NB grid points with 176 grids, and 541 million NB and OB grid points. Figure 19 shows the top view of the surface grids of the SUI quadcopter, with the names of the components.
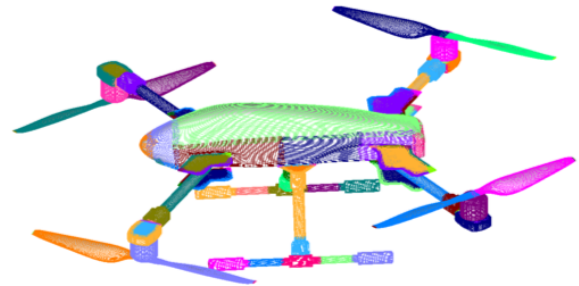

Figure 20: T-Motor P15x5 CF blades for the SUI Endurance. The top image shows a picture, the bottom image shows overset surface grids top view.

The rotor blades mounted on the SUI Endurance are the original T-Motor P15x5 CF blades; see figure 20. The geometry information was obtained by using high-resolution laser scanning conducted at NASA Ames. Airfoil profiles at different radii were generated from the point cloud, and the profiles were connected and smoothed, obtaining the whole blade. At the center, the blades were joined together without a hub. O-grids are used for the blades, and cap grids are generated for the blade tips.
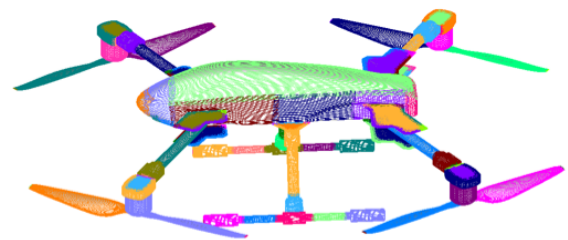
In order to study the effect of rotor mounting in

forward flight, three configurations of the SUI Endurance geometry have been modeled:

- Standard SUI, the conventional SUI Endurance configuration with the four rotors overmounted; see figure 21 (a).

- Hybrid SUI, the fore rotors are undermounted and the aft rotors remain overmounted,; see figure 21 (b).

- Undermount SUI, all rotors are undermounted; see figure 21 (c).
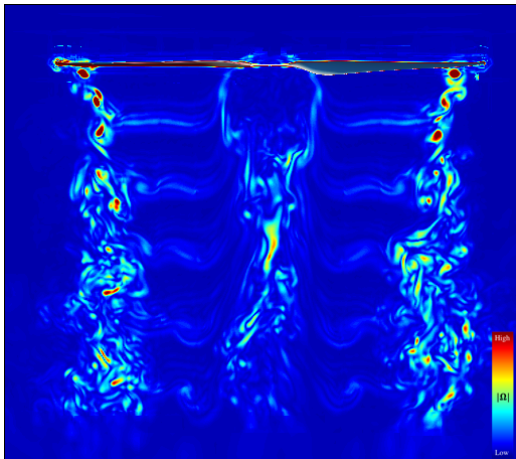
3.2.2. SUI Isolated Rotors

First, the SUI isolated rotor is simulated in hover. The rotational speed in hover is measured during tests and is equal to $\Omega_{hover} = 3600$ RPM.

Figure 22 shows the Q-criterion vorticity isosurfaces and the vorticity contours for the isolated

SUI rotor in hover. For Ω_{hover}, the tip Mach number is $M_{tip} = 0.2$ and the Reynolds number is $Re = 67500$.
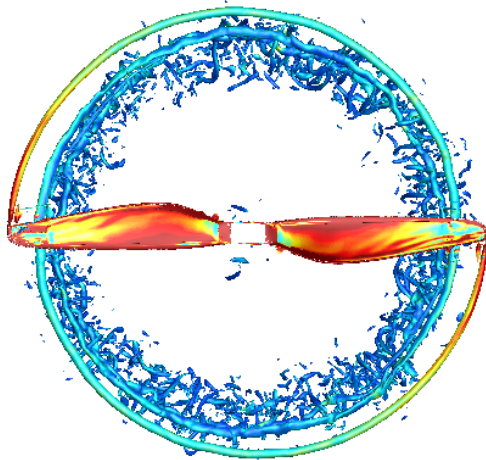
(a) Top view.

(b) Front view.

Figure 22: SUI isolated rotor in hover. Figure (a) shows the top view of the Q-criterion iso-surface colored by the vorticity. Figure (b) shows the vorticity magnitude, with pressure shown at the surface of the blades.

Table 3 shows the thrust coefficient, the torque coefficient, and the figure of merit obtained with Overflow for the SUI rotor. The coefficients are calculated as the mean value of their instantaneous values over the last three revolutions.

	SUI CF original blades
C_T	0.0092
C_Q	0.0013
FM	0.474

Table 3: SUI Endurance isolated rotor performances.

Excellent agreement is found with experimental results, as seen in figure 23. This figure shows C_T as a function of Ω. Experimental data was obtained from Zawodny et al.[15].
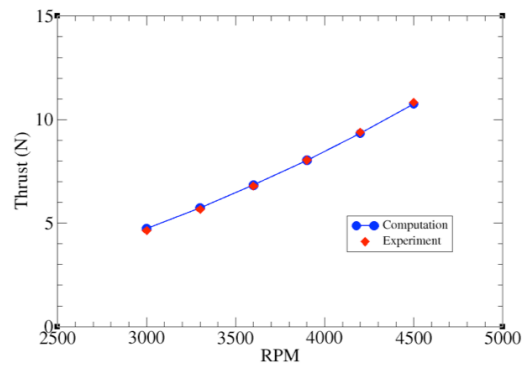

Figure 23: Comparison with experimental data for the SUI Endurance T-Motor rotors for various RPMs.

### 3.2.3. Effect of Rotor Mounting in Forward Flight

The SUI endurance design is improved for forward flight. The airplane-like fuselage and the canards have low drag and contribute to the lift in forward flight, even for small negative angles of attack. Quadcopters, like helicopters, need to have a negative angle of attack $\alpha < 0$ in order to generate forward force. With a negative α the rotor disk plane is leaning with a horizontal component generating a forward force to overcome the drag and a vertical component contributing to the lift in order to balance the weight.

The forward flight conditions simulated match the conditions of the flight tests conducted. The flow velocity is $V_\infty = 10\ m/s$, $\alpha = -7.7°$. Trim conditions were measured for the SUI standard vehicle. Fore and aft rotors rotate at different rotational speeds for the quasi-steady forward flight condition, $\Omega_{fore} = 3510$ RPM and $\Omega_{aft} = 4410$ RPM. The advance ratio based on the fore rotors is $\mu = 0.142$.

Figure 24 shows the results for the SUI quadcopter in forward flight. Rotor-rotor interactions are strong as the wakes of the fore rotors merge into those of the aft rotors. Supertip vortices from both fore and aft rotors are visible. The inboard supertip vortices from the fore rotors interact with the fuselage and then are fed into the advancing side of the aft rotors near the juncture of the fuselage and the aft canards. There are some blade-vortex interactions in the fore rotors. The aft rotors generate approximately 30% higher thrust than the fore rotors. Figure 25 (a) shows the velocity magnitude contours for the standard SUI vehicle.
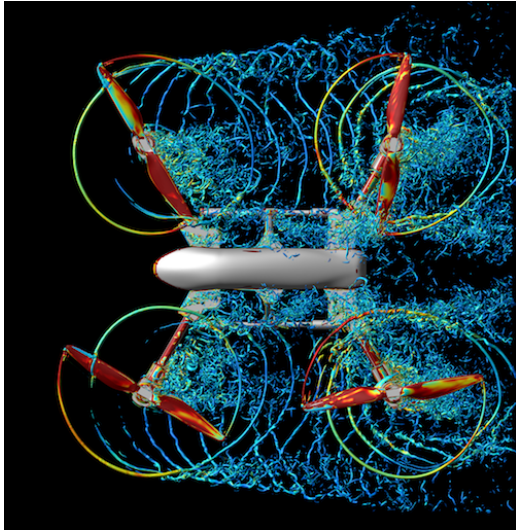
(a) Top view.
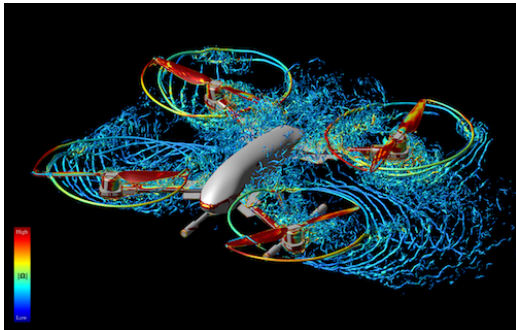
(b) Oblique view.

Figure 24: SUI quadcopter in forward flight. Figure (a) shows the top view of the Q-criterion iso-surface colored by the vorticity. Figure (b) shows an oblique view of the Q-criterion iso-surface colored by the vorticity.

With the idea of increasing the thrust of the aft rotors, the authors decided to undermount the fore rotors and keep the aft rotors overmounted, to obtain what it has been called a *hybrid configuration*. With this new arrangement, the aft rotors are no longer immersed in the wake of the fore rotors; see figure 25 (b). As a consequence, the thrust from the aft rotors increases substantially. The fore rotors thrust decreases slightly as a result of undermounting them, as observed in the DJI sections. However, the increase in aft-rotor thrust is much more important than the decrease in the fore-rotor thrust[‡]. We can conclude that the hybrid SUI is more efficient

[‡]New trim conditions would need to be found for the modified configurations. Because the thrust of the rotors changes, the rotational speed should be adjusted accordingly in order to keep the same quasi-steady forward flight condition. Still, the aft rotors are more efficient because they are no longer in the wake of the fore rotors.

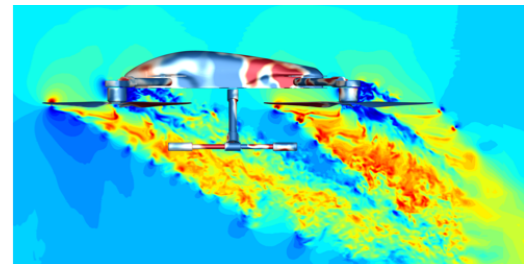aerodynamically than the standard configuration.

Finally, one last SUI vehicle has been simulated, the undermount SUI, see figure 25 (c). The download from the arms is important for overmounted rotors, and the objective of the undermount SUI is to reduce this effect.
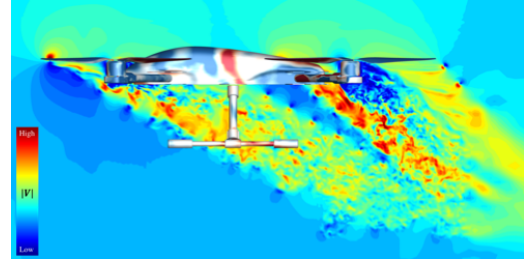
(a) Standard SUI.
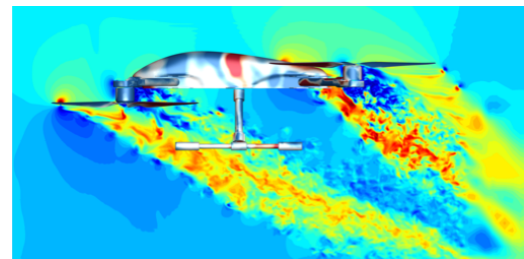
(b) Hybrid SUI.

(c) Undermount SUI.

Figure 25: SUI quadcopter in forward flight. Figure (a) shows the standard SUI, (b) shows the hybrid SUI, and (c) shows the undermount SUI. Note the interactions rotor-rotor for the standard and undermount configurations. Pressure shown at the surface.

Tables 4 and 5 show the performance of each component. The thrust/lift coefficient is decomposed into its horizontal part, c_x, and its vertical part c_y, for each component of the vehicle, as it can be seen in figure 26. Note that the factor dividing the forces is the same as with the thrust coefficient: $\rho(\Omega_{fore}R)^2 A$, without the "1/2" as in common use in lift and drag coefficients. The final values displayed have been normalized by 4x the thrust of the isolated rotor in hover.

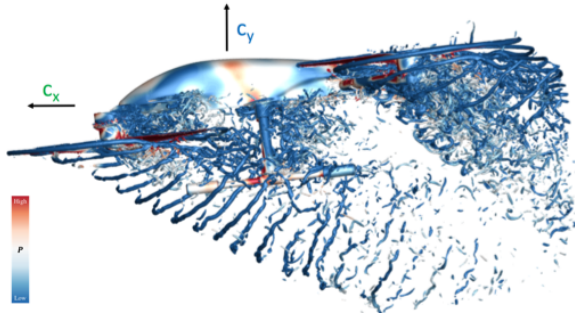First, when comparing the horizontal forces c_x, where negative values indicate drag, one can ob-

Figure 26: Hybrid SUI quadcopter in forward flight. Schematic of the force coefficients acting on the quadcopter, c_x and c_y.

c_y	Standard	Hybrid	Undermount
Fore rotors	0.633	0.631	0.629
Aft rotors	0.836	0.885	0.828
Fuselage	0.042	0.022	0.015
Landing gear	0.002	0.002	0.002
Canards	0.051	0.014	0.011
Arms	-0.046	-0.049	-0.027
TOTAL	1.517	1.504	1.436

Table 5: SUI Endurance quadcopter vertical force coefficient c_y in forward flight. Comparison of the horizontal forces acting on each component. Forces $F_{y,i}$ have been normalized by $\rho(\Omega_{fore}R)^2 A$ and then by 4x the thrust of the isolated SUI rotor in hover.

serve the increase in performance of the fore rotors in the hybrid case. Interactions with the aft rotors are minimal, and it seems that undermounting the rotors is beneficial in the SUI configuration, as the aft rotors undermounted are slightly better than in the standard case. The drag of the fuselage and landing gear is similar in all cases, smoothly increasing from the standard case to the undermount case. In the case of the canards, this effect is more noticeable. The standard SUI canards contribute positively to the forward force, but when the rotors are undermounted canards switch sign and contribute to the drag. One of the main actors in horizontal forces are the arms. Placing the rotors underneath decreases the drag of the arms substantially. Adding all components makes the hybrid the best configuration for forward flight, with an improvement of 63% in c_x.

c_x	Standard	Hybrid	Undermount
Fore rotors	0.053	0.056	0.055
Aft rotors	0.075	0.079	0.080
Fuselage	-0.003	-0.004	-0.005
Landing gear	-0.015	-0.019	-0.020
Canards	0.003	-0.002	-0.008
Arms	-0.091	-0.075	-0.070
TOTAL	0.022	0.036	0.033

Table 4: SUI Endurance quadcopter horizontal force coefficient c_x in forward flight. Comparison of the horizontal forces acting on each component. Forces $F_{x,i}$ have been normalized by $\rho(\Omega_{fore}R)^2 A$ and then by 4x the thrust of the isolated SUI rotor in hover.

In the case of the vertical forces c_y, the fore rotors are better when they are overmounted, as seen in the DJI cases. The aft rotors perform the best in the hybrid case, thanks to the reduction of interactions with the fore rotors. The fuselage generates some vertical force, contributing the most in the standard case, probably due to the low pressure regions below the rotors near the fuselage. This effect is lowered when the rotors are undermounted. The effect of the landing gear is not very important. The canards provide significant vertical force in the standard configuration. Again as with the fuselage, their contribution to vertical force is diminished when the rotors are placed underneath the arms. Download from the arms is similar between the standard and the hybrid cases. Fully undermounting the rotors reduces the download force. In total, the standard case has the highest lift but very close to the hybrid SUI, with just a difference of 1%.

Overall, the performance of the hybrid SUI is better than the two other configurations. A hybrid quadcopter is more efficient aerodynamically in forward flight than a fully overmount or undermount quadcopter.

3.3. The Eytron 4S UAV

The Elytron 4S UAV has a joined wing: the forward and aft wings are joined together by winglets, forming a "box-wing". Theoretically, the joined wing of the Elytron should decrease the induced drag. A full study of the Elytron 4S UAV can be found in previous work[2], where some configurations and flight conditions do indeed reduce the wing-tip vortices.

The components of the Elytron 4S UAV are shown in figure 27. It is a complicated configuration with three sets of wings, propellers, and a nose fan. The geometry modeling and aerodynamics of the vehicle are explained in the next sections.

3.3.1. Overset Grids

The geometries for the Elytron 4S UAV, the proprotors, and the nose fan have been provided by Elytron Aircraft LLC to NASA Ames as a STL CAD tri-
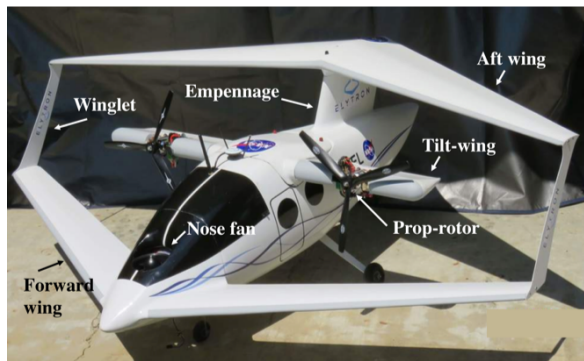
Figure 27: Elytron 4S UAV components.

(a) Top view. (b) Side view.

Figure 29: Elytron 4S UAV nose fan overset surface grids. Figure (a) shows a top view; figure (b) shows a side view. The fan is placed inside a hole near the nose, for pitch control during take-off and landing.

angulation. They can be imported directly into CGT, and then the overset grids are generated.

The Elytron prop-rotor grid system consists of three blades attached to a central hub. O-grids are used for the blades. Cap grids are generated for the blade tips and the hub ends. At the blade-hub junctions, collar grids are employed. Figure 28 shows the propeller overset surface grids.
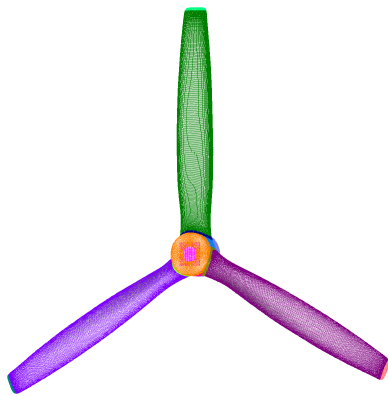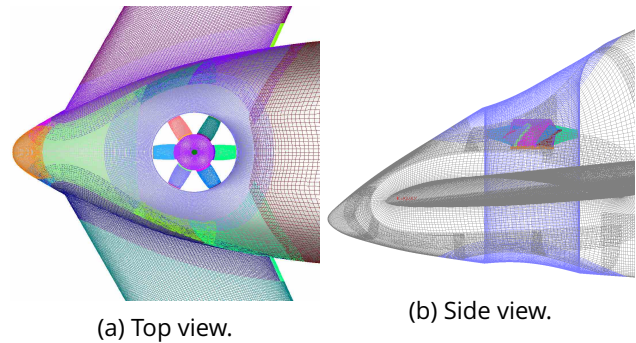

Figure 28: Elytron 4S UAV propeller overset surface grids.

The nose fan grids consist of six blades attached to a hub. O-grids are used for the blades. Cap grids are generated for the blade tips and the hub ends. In the blade-hub junctions, collar grids are employed. Figure 29 shows the surface grids for the nose fan and hole.

At the wing-fuselage junction, wing-winglet junctions, and wing-vertical empennage junction, collar grids are employed. O-grids have been used for all wings with high clustering around the trailing edge in order to solve the wakes and high clustering at the leading edge to accurately represent the curvature changes. Figure 30 shows the overset surface grids of the complete vehicle.

There are 147 NB grids with a total of 361 million NB and OB grid points.
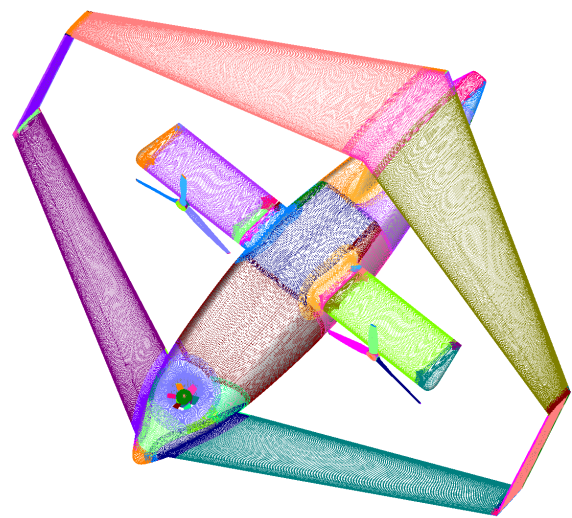

Figure 30: Elytron 4S UAV complete vehicle overset surface grids.

3.3.2. Aerodynamic Analysis of the Elytron

The Elytron 4S UAV has been simulated in forward flight, with the tilt-wing in "airplane mode" (tilt angle 0°), and in VTOL out of ground effect, with the tilt-wing in "helicopter mode" (tilt angle 90°). Table 6 shows the different flight conditions tested in the wind tunnel.

In this study, we are showing the CFD results using Overflow for the following flight conditions:

- Forward flight, with a freestream velocity $V_\infty = 67\ ft/s$, a static fan $N_{FAN} = 0$ RPM, for medium and high propeller rotational velocities $N_{PROP} = 6500$ RPM and $N_{PROP} = 7200$ rpm, and for angles of attack of AoA= 0° and AoA= 10°.

- Vertical Take-Off and Landing (VTOL) out of ground effect, with a propeller rotational veloc-

Flight mode	Forward flight	VTOL
N_{FAN} [RPM]	0	37000
N_{PROP} [RPM]	5800, 6500, 7200	9000
AoA [°]	0, 2.5, 5, 7.5, 10	0
V_{∞} [ft/s]	67	0
Tilt angle [°]	0	90

Table 6: Elytron 4S UAV flight conditions tested in wind tunnel.

ity of $N_{PROP} = 9000$ RPM and a fan rotational velocity of $N_{FAN} = 37000$ RPM.

The design of the box-wing reduces the induced drag and enhances structural stiffness. The effect of having joined wings with oversized winglets decreases the wingtip vortices and creates a larger effective aspect ratio, reducing the drag. With the tilt-wing concept, there is no retreating blade problem as in helicopter rotor blades in forward flight. This allows the vehicle to fly faster as the rotor blade will not suffer from dynamic stall.

Forward Flight

In forward flight, the nose fan is static. Figure 31 shows the Q-criterion vorticity iso-surfaces and the pressure at the surface for flight conditions $V_{\infty} = 67\ ft/s$, $N_{PROP} = 6500$ rpm and $N_{FAN} = 0$ rpm, with an AoA of $\alpha = 0°$ in (a) and $\alpha = 10°$ in (b).

The complicated configuration of the Elytron with a joined wing, empennage, and tilt-wing with its multiple junctures, is the source of many vortices:

- Wingtip vortices at the junction of the winglet with the aft wing.

- Wingtip vortices at the junction of the winglet with the forward wing.

- Wingtip vortices at the tip of the tilt-wing.

- Vortices at the junction of the tilt-wing with the fuselage.

- Vortices at the junction of the empennage with the aft wing.

- Horseshoe vortices at the junction of the forward wing, the tilt-wing, and the empennage with the fuselage.

A wingtip vortex is generated at the tip of the wing due to the difference in pressure between the lower surface (pressure side) and the upper surface (suction side). Air flows from below the wing and out around the tip to the upper surface of the wing in a circular fashion, producing the wingtip vortex.
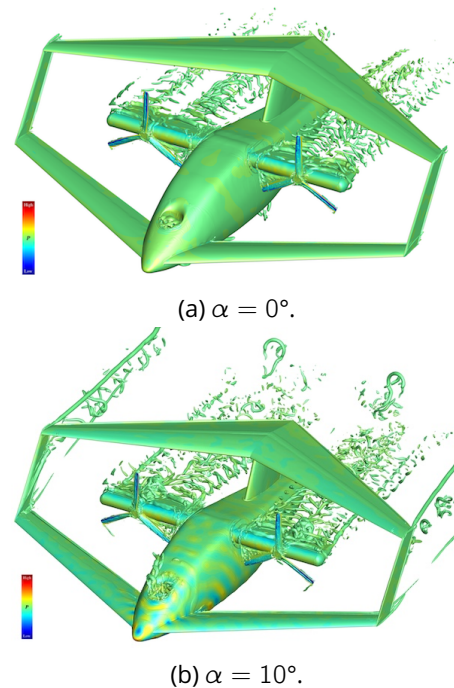

(a) $\alpha = 0°$.

(b) $\alpha = 10°$.

Figure 31: Q-criterion vorticity iso-surfaces and body surface pressure in forward flight at $V_{\infty} = 67\ ft/s$, $N_{PROP} = 7200$ RPM and $N_{FAN} = 0$ RPM, $\alpha = 0°$ in (a), and $\alpha = 10°$ in (b) for the Elytron 4S UAV, oblique view.

In fact, according to lifting-line theory, vorticity is trailed at any point on the wing where the lift varies span-wise; it eventually rolls up into large vortices near the wingtip, at the edge of flap devices, or at other abrupt changes in wing planform. That is, a vortex is generated whenever there is a change in lift span-wise. Wingtip vortices at the aft and forward wings are due to the change in lift close to the tip. The strength of the vortex at the tip of the tilt-wing is relatively weak and is not visible in the figures.

The vortices at the juncture of the tilt-wing with the fuselage are possibly caused by the horseshoe vortices of the junction and the small gap between the two wing sections. This small gap between the two sections of the tilt-wing is necessary in order to rotate the tilt-wing to transition from VTOL to forward flight and vice versa.

A vortex generated at the tip of the blade of a propeller is called the bladetip vortex. This vortex can interact with the next incoming blade, producing what is called Blade-Vortex Interaction (BVI). That is, BVI occurs when a rotor blade passes close to the shed tip vortices from a previous blade. This causes a rapid, impulsive change in the loading on
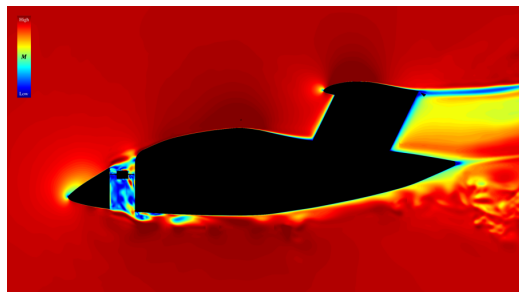
(a) $\alpha = 0°$.
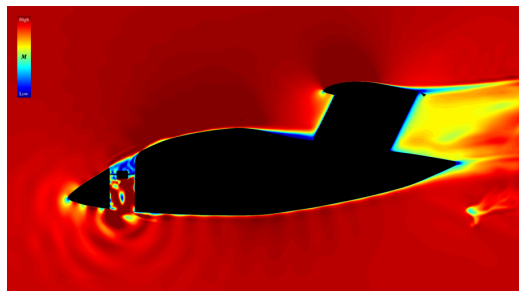
(b) $\alpha = 10°$.

Figure 32: Mach number in forward flight at $M_\infty = 0.06$ of the Elytron 4S UAV, side view.

the blade, resulting in the generation of highly directional impulsive loading noise.

For the Elytron in forward flight with the tilt-wing in airplane mode, there are no retreating blade problems[§]. The bladetip vortices interact with the tilt-wing and go downstream. BVI is not very important, as the vortices are carried downstream by the freestream velocity and do not interact with the following blade.

The wingtip vortices are relatively weak for AoA= 0°, thanks to the joined wing design. However, the wingtip vortices are more important for an AoA= 10°. The wingtip vortices at the junctions of the aft wing-winglets are relatively stronger than those at the junctions of the forward wing-winglets.

Figure 32 shows the Mach number M on a slice at $y = 0$, where the surface of the Elytron has been hidden in order to visualize clearly the interior of the hole, for AoA= 0° and AoA= 10°.

At an AoA= 0° the air flow inside the hole is partially blocked thanks to the static fan, but there is some vortex shedding underneath the fuselage, as seen in Figures 31 (a) and 32 (a).

For an angle of attack of AoA= 10°, the flow

[§]Retreating blade stall is a hazardous and damaging flight condition in helicopters, where the rotor blade on the retreating side of the rotor disc in forward flight, and therefore with the smaller resultant relative wind, exceeds the critical angle of attack. Retreating blade stall is one of the primary limiting factors in a helicopter's airspeed and the reason even the fastest helicopters can only fly slightly faster than 200 knots.

inside the hole is almost totally blocked, as seen in Figure 32 (b) by the low velocity region above the fan. However, inside the hole, below the fan, the flow is contained but fluctuating, generating the propagation of pressure waves. The fluctuations are stronger than for AoA= 0°. In addition, as flow through the hole is almost totally blocked by the static fan, flow is spilled out of it above the fuselage, producing vortices, as seen in figure 31 (b).

Vertical Take-Off and Landing
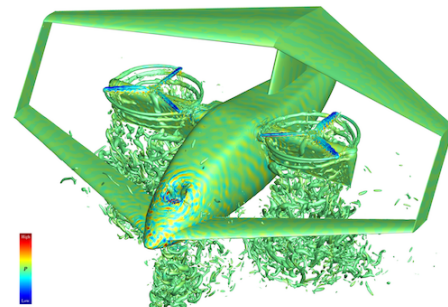

(a) Oblique view.
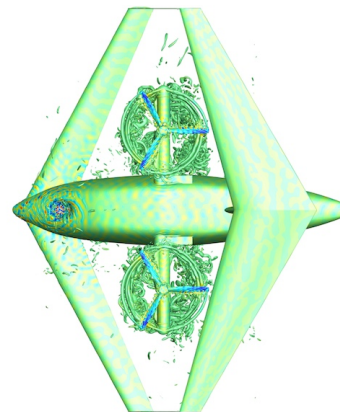
(b) Top view.

Figure 33: Q-criterion vorticity iso-surfaces and body surface pressure in VTOL out of ground effect with $N_{PROP} = 9000$ RPM and $N_{FAN} = 37000$ RPM for the Elytron 4S UAV. The tilt-wings are tilted 90° so the thrust from the propellers is vertical.

Figure 33 shows the rotor wakes and the instantaneous surface pressure on the body for the Elytron 4S UAV in VTOL out of ground effect. The conditions simulated have the propellers and fan rotating at maximum rotational velocity, $N_{PROP} = 9000$ RPM and $N_{FAN} = 37000$ RPM. During take-off and landing, the tilt-wing is tilted 90° for VTOL.

With the wing in helicopter mode and no freestream velocity, there is BVI. The vortices shed from the previous blade pass very close to the next blade. This causes a rapid change in the loading of

(a) $y = 0$ slice.
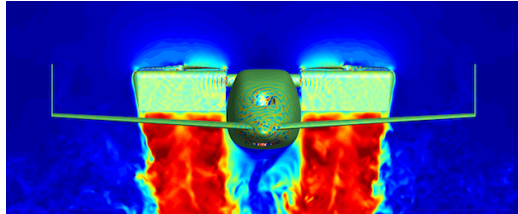
(b) $x = constant$ slice.

Figure 34: Mach number in VTOL out of ground effect at $M_\infty = 0.06$ of the Elytron 4S UAV.

(a) Quadrotor concept.

(b) Side-by-side concept.

(c) Tilt-wing concept.

Figure 35: NASA's UAM conceptual designs.

Figure 36: NASA's UAM conceptual designs.

the blade, producing noise. Also, the vortices interact further downstream with the tilt-wing, which is immersed in their wake, creating another source of noise. The cabin must be very well sound-insulated in order to be able to carry passengers.

The nose fan high rotational velocity produces high frequency pressure fluctuations, as seen in Figure 33. In this figure one can also clearly see the vortex wakes from the nose fan and the propellers.

Figure 34 shows the Mach number contours at $y = 0$ and at $x = constant$ slices.

3.4. NASA's Side-by-Side UAM Helicopter

New concept vehicles are intended to focus and guide NASA research activities in support of aircraft development for emerging markets, in particular VTOL air taxi operations[5].

Figure 35 shows NASA's conceptual designs for UAM, (a) shows a single passenger quadcopter, (b) shows a six passenger side-by-side helicopter, and (c) shows a fifteen passenger tilt-wing helicopter. Many other designs are being explored with Multidisciplinary Design, Analysis, and Optimization (MDAO) techniques[16], as shown in figure 36.
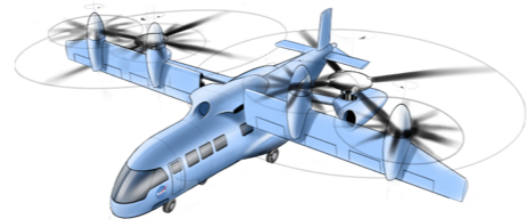
The side-by-side conceptual design is being studied using high-fidelity CFD. Low-fidelity simulation tools have shown an improvement in the efficiency of cruise flight for a rotor overlap of 15%[16].

3.4.1. Overset Grids

The fuselage geometry has been developed using MDAO. The blade planform and twist, sweep and droop of the tip are optimized using comprehensive analysis.

Figure 37 shows the rotors overset surface grids for the side-by-side helicopter. There are two overlapping rotors with four blades each.

The complete vehicle is shown in figure 38. There are 131 NB grids with 75 million NB grid points and 431 million NB and OB grid points.
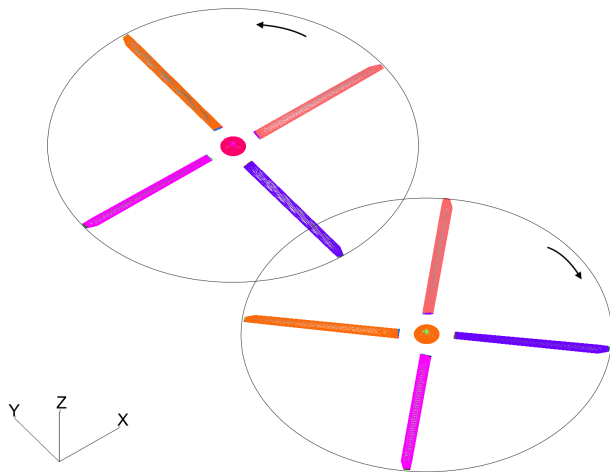
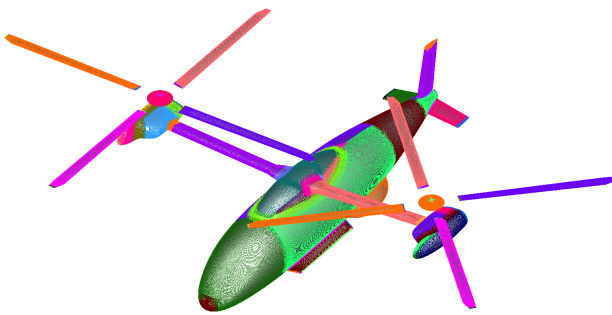Figure 37: Overset surface grids for the side-by-side rotors.

Figure 38: Overset surface grids for the side-by-side vehicle with rotors.

3.4.2. Overlapping Intermeshing Rotors in Hover

The rotational speed in hover for the side-by-side helicopter is $\Omega_{hover} = 444$ RPM. The Reynolds number is $Re = 1476600$, and the Mach number at the tip is $M_{tip} = 0.49$. Some preliminary results are shown here for the two overlapping rotors. The complete study is work in progress.

Some interesting results have already been obtained, see figure 39. As expected, two overlapping rotors lose efficiency in hover, due to interference in the overlapping region. Figure 39 shows the velocity magnitude; note the higher downwash where the rotors intermesh. In figure 39 (b) the complex structures of the vortices can be seen.

4. SUMMARY

High-order accurate Computational Fluid Dynamics simulations have been carried out for several multi-rotor vehicles. NASA's supercomputers Pleiades and
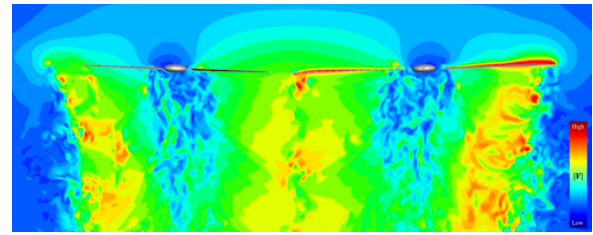
(a) Velocity magnitude.
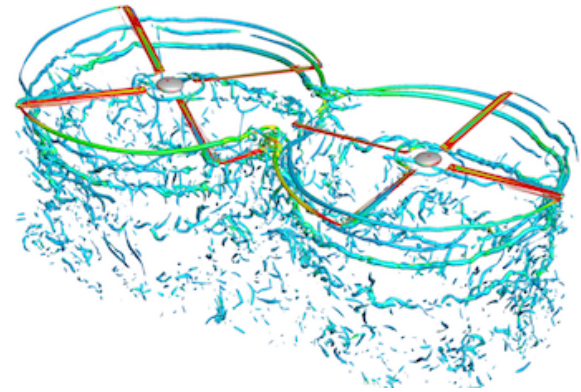
(b) Q-criterion.

Figure 39: Side-by-side intermeshing rotors. Figure (a) shows the velocity magnitude. Figure (b) shows the Q-criterion iso-surfaces colored by the vorticity magnitude.

Electra were essential for this work as the overset grids have hundred of millions of grid points.

First, a complete study of the DJI Phantom 3 and its variants in hover has been carried out. Better designs of blades generate more thrust more efficiently. The effects of over- and under-mounting the rotors have been studied, concluding that under-mounting the rotors reduces the thrust and produces stronger pressure fluctuations. An octorotor increases the thrust but also the power required to fly it. Components may reduce the interactions among the rotors but the airframe download increases. Therefore they should be placed carefully in order to reduce the download force. Simulations of wind gusts have shown that a dissymetry in rotor thrust produces a pitching moment that will unstabilize the quadcopter. The effect is stronger for higher wind gust speeds.

The SUI Endurance simulations in forward flight have thrown insight on better designs during cruise: under-mounting the fore rotors and over-mounting the aft rotors improves the aerodynamic efficiency of the vehicle, by reducing the interactions between the fore and aft rotors. The so called *hybrid SUI* increases the forward horizontal force by 63% compared to the standard SUI.

The aerodynamic analysis of the Elytron 4S UAV

shows the complicated juncture flows and vortices due to the multiple components. Wingtip vortices for small angles of attack are relatively weak, but they get stronger as the angle of attack increases. Vortex shedding is seen underneath the fuselage for AoA = 0 and on top of the fuselage for AoA = 10. With a static fan inside the hole, the air flow is partially blocked through the hole, but it still introduces pressure fluctuations. In VTOL out of ground effect, the nose fan rotates at maximum velocity, producing high-frequency pressure fluctuations. The nose fan is used for pitch control, and BVI can be observed for the propeller blades.

Finally, NASA's new concepts for UAM have been introduced. These concept vehicles are expected to focus and guide NASA research activities in support of aircraft development for emerging aviation markets, in particular VTOL air taxi operations. Preliminary results for the side-by-side configuration have been presented.

ACKNOWLEDGMENTS

REFERENCES

[1] Ventura Diaz, P., and Yoon, S., "High-Fidelity Computational Aerodynamics of Multi-Rotor Unmanned Aerial Vehicles", AIAA Paper 2018-1266, The AIAA SciTech Forum 2018, Kissimmee, Florida, Jan. 2018.

[2] Ventura Diaz, P., Yoon, S., and Theodore, C. R., "High-Fidelity Computational Aerodynamics of the Elytron 4S UAV", The AHS International Technical Meeting on Aeromechanics Design for the Transformative Flight, San Francisco, California, Jan. 2018.

[3] Yoon, S., Ventura Diaz, P., Boyd, D. D., Chan, W. M., and Theodore, C. R., "Computational Aerodynamic Modeling of Small Quadcopter Vehicles", AHS Paper 73-2017-0015, The 73rd Annual AHS International Forum & Technology Display, Fort Worth, Texas, May 2017

[4] Yoon, S., Chan, W. M, and Pulliam, T. H., "Computations of Torque-Balanced Coaxial Rotor Flows", AIAA Paper 2017-0052, The 55th AIAA Aerospace Sciences Meeting, Grapevine, Texas, January 2017.

[5] Johnson, W., Silva, C., and Solis, E., "Concept Vehicles for VTOL Air Taxi Operations", The AHS International Technical Meeting on Aeromechanics Design for the Transformative Flight, San Francisco, California, Jan. 2018.

[6] Pulliam, T. H., "High Order Accurate Finite-Difference Methods: as seen in OVERFLOW", AIAA Paper 2011-3851, June 2011.

[7] Chan, W. M., Gomez, R. J., Rogers, S. E., Buning, P. G., "Best Practices in Overset Grid Generation", AIAA Paper 2002-3191, The 32nd AIAA Fluid Dynamics Conference, St. Louis, Missouri, June 2002.

[8] Yoon, S. Lee, H. C., and Pulliam, T. H., "Computational Study of Flow Interactions in Coaxial Rotors", The AHS Technical Meeting on Aeromechanics Design for Vertical Lift, San Francisco, California, Jan. 2016.

[9] Yoon, S., Chaderjian, N. M., Pulliam, T. H., and Holst, T. L., "Effect of Turbulence Modeling on Hovering Rotor Flows", AIAA Paper 2015-2766, The 45th AIAA Fluid Dynamics Conference, Dallas, Texas, June 2015.

[10] Jespersen, D., Pulliam, T. H., and Buning, P., *Recent Enhancements to OVERFLOW*, AIAA Paper 97-0644, Reno, Nevada, Jan. 1997.

[11] Lakshminarayan, V. K., and Baeder, J. D., *Computational Investigation of Micro Hovering Rotor Aerodynamics*, Journal of the American Helicopter Society, 55, 022001, 2010.

[12] Spalart, P. R., Jou, W-H., Strelets, M., and Allmaras, S. R., "Comments on the Feasibility of LES for Wings and on a Hybrid RANS/LES Approach", Advances in DNS/LES, Greyden Press, 1997, pp. 137-147.

[13] Spalart, P. R., "Strategies for Turbulence Modeling and Simulations", International Journal of Heat and Fluid Flow, 21, 2000, pp. 252-263.

[14] Russell, C.,"Wind Tunnel and Hover Performance Test Results for Multicopter UAS Vehicles", NASA/TM–2018–219758

[15] Zawodny, N. S., Boyd, D. D., and Burley, C. L., "Acoustic Characterization and Prediction of Representative, Small-Scale Rotary-Wing Unmanned Aircraft System Components", The 72nd AHS Annual Forum, West Palm Beach, Florida, May 2016.

[16] Silva, C., Johnson, W., and Solis, E., "Multidisciplinary Conceptual Design for Reduced-Emission Rotorcraft", The AHS International Technical Meeting on Aeromechanics Design for the Transformative Flight, San Francisco, California, Jan. 2018.